Posted on 24 Nov 2022 — The copyright holder is the author/funder. All rights reserved. No reuse without permission. — https://doi.org/10.1002/essoar.10512160.1 — This a preprint and has not been peer reviewed. Data may be preliminary.

A Dynamic Pathway by which Northern Hemisphere Extratropical Cooling Elicits a Tropical Response

Matthew Luongo[1], Shang-Ping Xie[2], Ian Eisenman[3], Yen-Ting Hwang[4], and Hung-Yi Tseng[4]

[1]University of California, San Diego
[2]UCSD
[3]UC San Diego
[4]National Taiwan University

November 24, 2022

Abstract

Previous studies have found that Northern Hemisphere aerosol-like cooling induces a La Nina-like quasi-equilibrium response in the tropical Indo-Pacific. Here, we explore a coupled atmosphere-ocean feedback pathway by which this response is communicated. We override ocean surface wind stress in a comprehensive climate model to decompose the total ocean-atmosphere response to forced extratropical cooling into the response of surface buoyancy forcing alone and surface momentum forcing alone. In the subtropics, the buoyancy-forced response dominates: the positive low cloud feedback amplifies sea surface temperature (SST) anomalies which are then communicated to the tropics via wind-driven evaporative cooling. In the deep tropics, the momentum-driven Bjerknes feedback creates zonally asymmetric SST patterns in the Indian and Pacific basins. Although subtropical cloud feedbacks are model-dependent, our results suggest this feedback pathway is robust across a suite of models such that models with a stronger subtropical low cloud response exhibit a stronger La Nina response.

A Dynamic Pathway by which Northern Hemisphere Extratropical Cooling Elicits a Tropical Response

Matthew T. Luongo[1], **Shang-Ping Xie**[1], **Ian Eisenman**[1], **Yen-Ting Hwang**[2], **&** **Hung-Yi Tseng**[2]

[1]Scripps Institution of Oceanography, UC San Diego, La Jolla, CA
[2]Department of Atmospheric Sciences, National Taiwan University, Taipei, Taiwan

Key Points:

- A pathway of three coupled ocean-atmosphere feedbacks communicates extratropical anomalous cooling and creates a tropical response
- Broadly, buoyancy-forced adjustments dominate in the subtropics while momentum-forced adjustments create zonal asymmetries in the tropics
- This mechanistic pathway seems to be robust across several GCMs

Corresponding author: M.T. Luongo, `mluongo@ucsd.edu`

Abstract

Previous studies have found that Northern Hemisphere aerosol-like cooling induces a La Niña-like quasi-equilibrium response in the tropical Indo-Pacific. Here, we explore a coupled atmosphere-ocean feedback pathway by which this response is communicated. We override ocean surface wind stress in a comprehensive climate model to decompose the total ocean-atmosphere response to forced extratropical cooling into the response of surface buoyancy forcing alone and surface momentum forcing alone. In the subtropics, the buoyancy-forced response dominates: the positive low cloud feedback amplifies sea surface temperature (SST) anomalies which are then communicated to the tropics via wind-driven evaporative cooling. In the deep tropics, the momentum-driven Bjerknes feedback creates zonally asymmetric SST patterns in the Indian and Pacific basins. Although subtropical cloud feedbacks are model-dependent, our results suggest this feedback pathway is robust across a suite of models such that models with a stronger subtropical low cloud response exhibit a stronger La Niña response.

Plain Language Summary

Anthropogenic aerosol emissions are an important radiative forcing on the climate system and partially explain observed climate variability. In prior modeling studies, idealized aerosol-like forcing applied to Northern Hemisphere high latitude regions has resulted in a tropical La Niña-like response in the Eastern Equatorial Pacific. In this study, we investigate the pathway by which high latitude aerosol-like cooling is communicated to the tropics via a sequence of ocean-atmosphere positive feedback processes. We explore this pathway further by introducing a protocol to parse out the total climate response into surface buoyancy-forced adjustments and surface momentum-forced adjustments. We find that subtropical patterns, arising from low clouds and turbulent heat fluxes, are primarily buoyancy-forced, and that tropical patterns are dominated by momentum-forced adjustments. Though cloud feedbacks can be highly variable across models, our results show that this pathway is robust across seven climate models such that stronger subtropical cloud responses elicit stronger sea surface temperature responses in the equatorial Pacific. Our results highlight the important link between extratropical aerosol-like forcing and El Niño-like patterns via these coupled ocean-atmosphere feedbacks. The equatorial Pacific can drive major climate variability suggesting global implications of these results.

1 Introduction

Extratropical atmospheric variability, either resulting from internal climate variability (e.g., Hasselmann, 1976; Chang et al., 2007) or in response to an anomalous forcing of the climate system (e.g., Kang et al., 2008; Hwang et al., 2017), can influence the tropics through coupled ocean-atmosphere interactions. Due to the global influence of the El Niño-Southern Oscillation (ENSO), extratropical forcing of ENSO variability is of particular interest. Many studies (e.g., Vimont et al., 2003; Chang et al., 2007; Larson & Kirtman, 2013, 2014; Lu et al., 2017; Pegion & Selman, 2017; Thomas & Vimont, 2016; Ma et al., 2017) have shown that variations in the the Pacific Meridional Mode (PMM: Chiang & Vimont, 2004; Amaya, 2019), the second leading mode of North Pacific ocean-atmosphere variability, can communicate extratropical variability to the tropics via the Wind-Evaporation-Sea Surface Temperature (WES: Xie & Philander, 1994) feedback. This stochastic extratropical forcing on the tropics may then excite the tropical Bjerknes feedback (Bjerknes, 1969) and develop into an El Niño or La Niña event.

While many studies have explored how interannual, extratropical variability can excite interannual, tropical variability (e.g., Nonaka et al., 2000, 2002), until recently few studies have focused on how the extratropics can excite a quasi-equilibrium tropical response. The Extratropical-Tropical Interaction Model Intercomparison Project (ETINMIP: Kang et al., 2019) seeks to understand the dynamic linkages between extratropical forcing and tropical responses via a coupled global climate model (GCM) framework. In ETINMIP, a zonally-uniform reduction in top-of-atmosphere (TOA) solar insolation is continuously applied to multiple GCMs in either the Northern Hemisphere (NH) or Southern Hemisphere (SH) extratropics. A La Niña-like pattern of sea surface temperature (SST) in the Pacific Ocean and a negative Indian Ocean Dipole (IOD)-like pattern of SST in the Indian Ocean is a robust response across models in the long-term, multi-model mean under both the NH and SH TOA forcing (Kang et al., 2019, 2020).

Kang et al. (2020) investigate the Walker circulation response to extratropical cooling in the presence and absence of dynamic ocean adjustment. When the ocean is allowed to dynamically adjust to forcing, they suggest that cooled subtropical waters upwell in the equatorial Pacific via the climatological subtropical cells (STCs: McCreary & Lu, 1994; Z. Liu, 1994); these cooler waters would create a zonal gradient in SST and strengthen the Walker Cell via the Bjerknes feedback. While this STC-focused thermocline pathway, sometimes referred to as the "oceanic tunnel" (Burls et al., 2017; Heede et al., 2020), is often invoked to explain how extratropical variability could theoretically excite tropical variability (Wang et al., 2018; Stuecker et al., 2020; England et al., 2020), the timescale of thermocline ventilation is potentially slower than the timescale for the La Niña response to develop (Nonaka et al., 2002).

In a complementary study, Tseng et al. (Submitted) explore the fast and slow responses of the tropical Pacific to extratropical forcing. They point to changes in STC strength and resulting anomalous meridional heat convergence, rather than changes in the temperature of upwelled waters, as the driver of the tropical Pacific quasi-equilibrium response that develops within ten years. The full mechanism of this subsurface STC adjustment remains to be determined. While prior studies pointed to changes in wind stress and resulting momentum-forced changes as the driver of STC adjustments, results from Luongo et al. (In Press) call into question this simple picture by showing that buoyancy-forced changes dominate the STC adjustment and corresponding cross-equatorial ocean heat transport response to NH extratropical cooling. Though this focus on the STC adjustment likely provides the precursor for this La Niña-like quasi-equilibrium response, it ignores an important pathway of additional coupled ocean-atmosphere processes which help amplify and maintain the long-term response throughout the tropical Indo-Pacific.

In this study we explore a pathway involving three coupled feedback processes by which NH extratropical cooling can elicit and sustain a La Niña-like quasi-equilibrium response in the tropical Pacific. We employ a series of wind stress locking experiments that were used in Luongo et al. (In Press) to partition the ocean's fully-coupled response into a buoyancy-forced and momentum-forced adjustment. We show that the subtropics are dominated by buoyancy-forced modes (section 3.1), while patterns in the tropics are primarily momentum-forced (section 3.2). We discuss what these wind stress locking simulations imply for tropical mode phase estimation (section 4.1) and the extent to which the proposed coupled process pathway is robust across ETINMIP member models (section 4.2). We conclude in section 5.

2 Experimental Design & Methods

2.1 GCM Simulations

We use the output from five simulations carried out with version 1.2.2 of the Community Earth System Model (CESM: Hurrell et al., 2013) in a standard, coupled pre-industrial configuration with atmosphere and land components run on a nominally 2° horizontal resolution and ocean and sea ice components run on a nominally 1° horizontal resolution. Briefly, we approximate the ocean's total response (fully-coupled: "FC") to a reduction in NH extratropical top-of-atmosphere (TOA) insolation (Figure S1) as the linear sum of the ocean's response to the change in surface buoyancy flux (buoyancy-forced: "BF") and the ocean's response to a change in surface wind stress (momentum-forced: "MF", i.e. FC $\approx$ BF + MF). See further simulation setup details in Luongo et al. (In Press).

To mechanistically decompose the ocean's response to surface buoyancy forcing alone and surface momentum forcing alone, we output wind stress from a freely evolving unforced control case and an ETINMIP-style NH TOA radiatively-forced case. We then override wind stress in three experiments, a decoupled and unforced control, a radiatively-forced experiment with unforced wind stress, and an experiment without radiative forcing but with prescribed forced winds. See Table S1 for simulation details. To address the effects of CESM's internal climate variability, we run three realizations of each of these five cases with slightly different initial conditions a là Kay et al. (2015) and present the ensemble mean of the three realizations throughout this study. We compare the freely-evolving FC response with that of the BF response and the MF response [Luongo et al. (In Press) evaluates the linear assumption and show that nonlinearities and decoupling effects are much smaller than the BF or MF responses]. Lastly, as we are interested in the quasi-steady state response of the ocean-atmosphere system in this paper, we focus on the average of the last 40 years of the 50-year simulations.

2.2 Ocean Mixed Layer Heat Budget

In order to attribute the dynamic drivers of specific SST patterns, we perform an energy budget analysis of the ocean mixed layer (e.g., Xie et al., 2010; Hwang et al., 2017):

$$\rho_0 C_p H \frac{\partial T}{\partial t} = Q'_{net} + D'_o = Q'_{SW} + Q'_{LW} + Q'_{SH} + Q'_{LH} + D'_o \ . \quad (1)$$

Above, the left-hand side is the product of seawater density (ρ_0, assumed to be constant), ocean heat capacity (C_p), mixed layer depth (H), and temperature tendency ($\partial T/\partial t$). The right-hand side is the sum of net surface heat flux perturbations, Q'_{net}, and horizontal divergence of three-dimensional ocean heat transport, D'_o, which includes advective and diffusive processes. Because $\partial T/\partial t$ is near zero in the quasi-equilibrium tropics and subtropics, this implies that the change in Q'_{net}, which is the sum of changes in shortwave (Q'_{SW}), longwave (Q'_{LW}), sensible (Q'_{SH}), and latent heat fluxes (Q'_{LH}), is approximately balanced by D'_o.

Based on the linear bulk formulation for evaporation, which dominates latent heat flux changes in the tropics and subtropics (i.e. $Q'_{LH} \approx -Q'_E$: see Figure S2), we can decompose latent heat flux changes into changes from variations in wind speed (W), relative humidity (RH), air-sea temperature gradient (S), and a Newtonian cooling term proportional to the SST anomaly. By normalizing by the product of the mean evaporative heat flux and a Clausius-Clapeyron scaling, we can write a diagnostic equation for SST anomalies in a region:

$$\begin{aligned} T' &= T'_{SW} + T'_{LW} + T'_{SH} + T'_{E,W} + T'_{E,RH} + T'_{E,S} + T'_{Do} \\ &\approx T'_R + T'_E + T'_{Do} \ . \end{aligned} \quad (2)$$

This decomposition allows us to diagnose the primary drivers of SST anomalies in specific regions (Figure S3) and identify leading dynamic modes of variability. Noting that tropical and subtropical sensible heat fluxes are small ($T'_{SH} \approx 0$, Figure S2-S3), we approximate the full decomposition as a sum of the radiative terms ($T'_R = T'_{SW} + T'_{LW}$, primarily driven by T'_{SW}), T'_{Do}, and the evaporative terms ($T'_E = T'_{E,WS} + T'_{E,RH} + T'_{E,S}$, primarily driven by $T'_{E,W}$). See Text S1 for a detailed derivation of Equation 2.

3 Extratropical-Tropical Dynamic Pathway

3.1 Buoyancy-Dominated Subtropics

Striking similarities in SST and near-surface wind patterns exist between the FC and BF Pacific and Atlantic NH subtropics (Figures 1a and 1b). These similarities em-

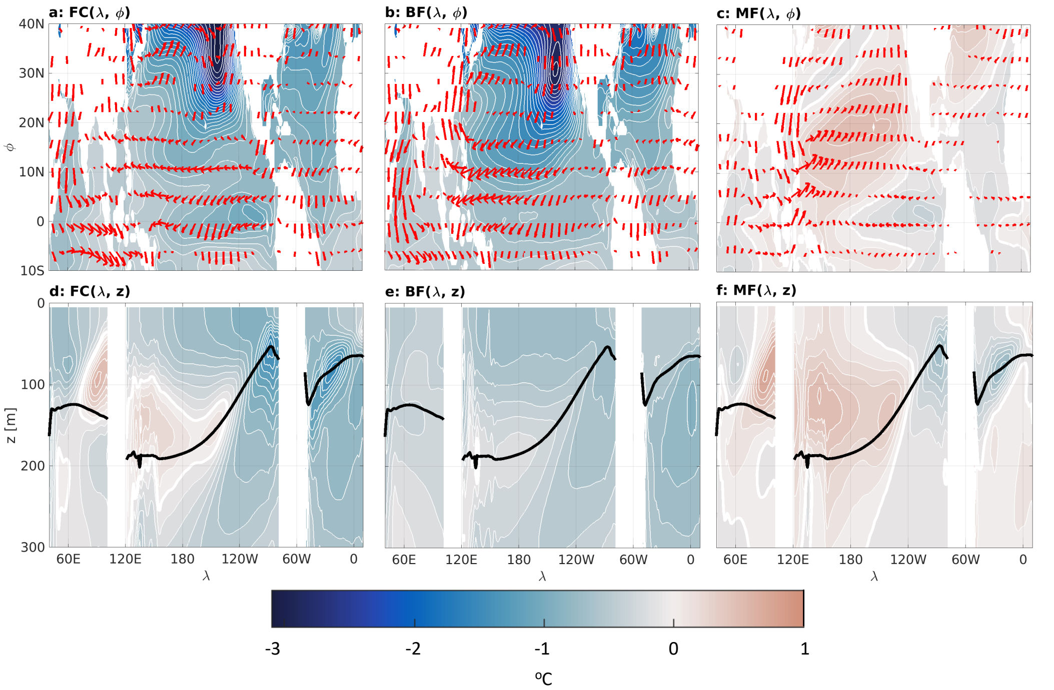

Figure 1. Top row: SST(λ, ϕ) for FC, BF, and MF (colorfill and white contours of 0.1 °C) with 850 hPa near-surface wind vectors. The SST zero contour is plotted as a thick white line. Bottom row: Equatorial (averaged over 5°S-5°N) temperature depth-profile (colorfill and white contours of 0.1 °C). The $\sigma_0 = 25$ kg m^{-3} isopycnal of the control state is plotted as a thick black line. The temperature zero contour is plotted as a thick white line.

phasize the extent to which buoyancy forcing dominates the total subtropical response of the ocean-atmosphere system. In the Pacific basin, a strong zonal SST gradient develops such that the eastern half of the basin is significantly cooler than the western half; in particular, SST perturbations are most highly negative below the marine stratiform cloud deck off the west coast of North America. In the marine stratocumulus regime, the positive low cloud feedback (Norris & Leovy, 1994; Norris et al., 1998; Clement et al., 2009; Wood, 2012; Hsiao et al., 2022) can amplify negative SST perturbations by increasing cloud cover, reducing solar insolation, and cooling local SSTs further. Figure S9 of Luongo et al. (In Press) demonstrates CESM's strong increase in low cloud cover and subsequent decrease in surface shortwave radiative forcing in both FC and BF; this decrease in solar forcing coincides with the amplified negative SST anomalies in the northeast subtropical Pacific seen in Figures 1a and 1b. We diagnostically attribute this cooling to the cloud cover increase through the mixed layer budget decomposition: Figure

2a shows that radiative forcing (T'_R), dominated by T'_{SW}, is the primary driver of total temperature change (T'). The low cloud driven shortwave radiative forcing effect drives negative SST anomalies in the Northeast Pacific low cloud deck, although wind speed driven changes (T'_E) also contribute to negative SST anomalies, whereas ocean heat transport (T'_{Do}) acts to warm SST.

In both FC and BF, these SST anomalies extend southwestward from the low cloud deck and resemble the familiar PMM pattern (Chiang & Vimont, 2004; Amaya, 2019), which propagates negative SST anomalies southwestward via the wind-evaporation-SST (WES) feedback (Xie & Philander, 1994). As expected from the WES feedback's dynamic mechanism, these PMM patterns are accompanied by basin-scale anti-cyclonic anomalous near-surface winds. Figure 2b shows that the PMM-like cooling observed in the subtropical western Pacific in FC and BF is driven by thermodynamic effects of wind speed on latent heat flux. It should be emphasized that our wind stress overriding protocol only overrides surface wind stress; rather than overriding total wind, MF isolates the Ekman adjustment while wind speed effects (e.g. for turbulent heat fluxes) are retained within BF. While other factors influence this region's total SST change, wind speed, and thus the WES feedback, is the largest driver of negative SST anomalies in the subtropical western Pacific where this PMM propagates. The fact that this cooling is communicated southwestward via a PMM is significant as these PMM winds can force the tropics with extratropical variability.

This agreement between FC and BF is in marked contrast to the MF case, which largely diverges from the FC response: momentum-forced adjustment leads to subtropical SST warming in both the Pacific and Atlantic basins (Figure 1c). In the Pacific, cyclonic wind anomalies reduce the strength of the climatological anti-cyclonic winds in the Pacific basin, decreasing both total wind speed and evaporative cooling, and subsequently warming the subtropical western Pacific (Figure 2b). This warming signal then propagates northeastward via WES in a positive phase of the PMM. The cyclonic near-surface response in MF tempers the strong anti-cyclonic BF response such that FC patterns resemble a weaker BF.

Though less coherent patterns exist in the Atlantic than the clear low cloud and PMM responses in the Pacific, the agreement between FC and BF subtropical Atlantic SST and near-surface wind is also strong. In both cases, cooling is concentrated in the

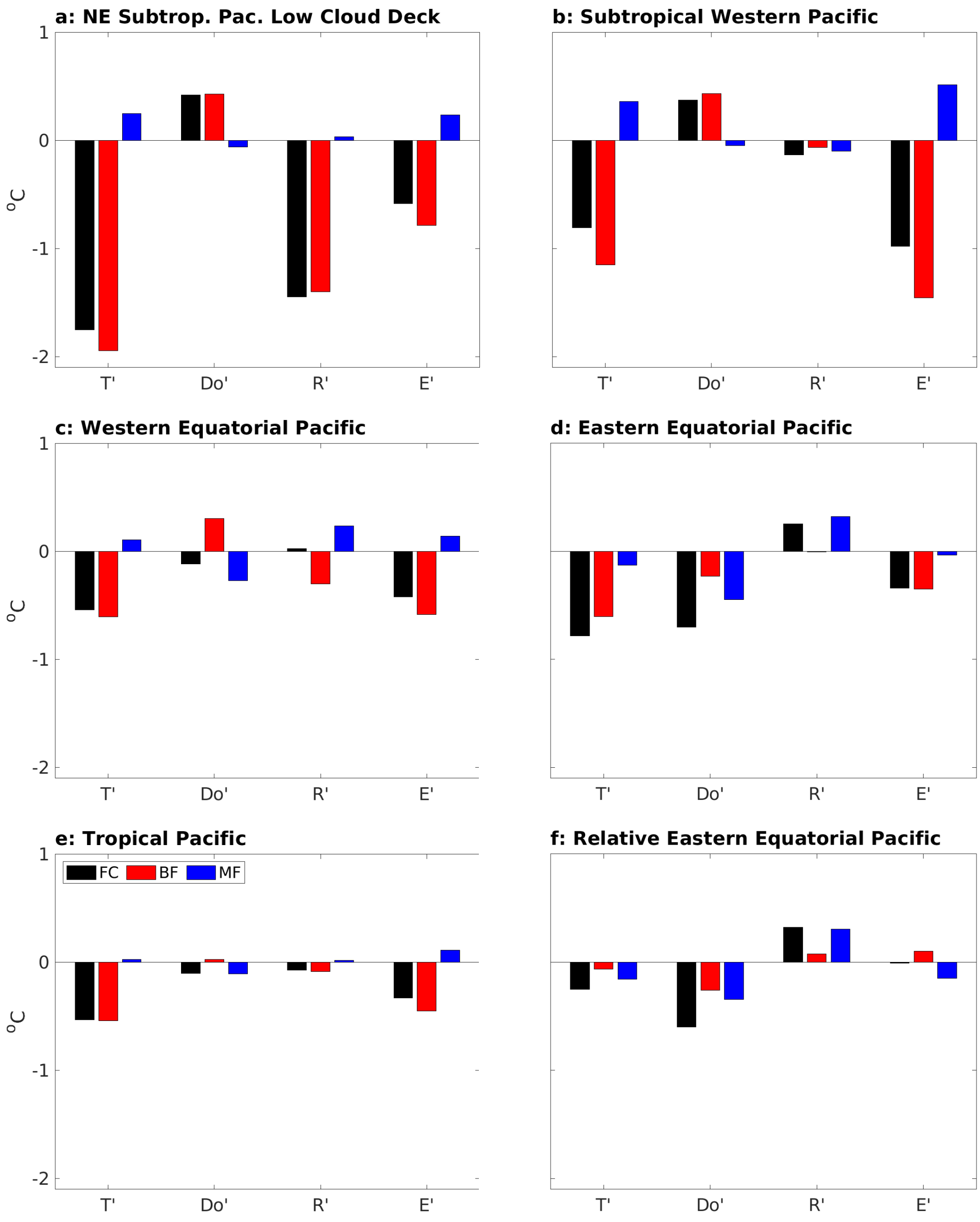

Figure 2. Ocean mixed layer SST diagnostic attribution presented in Equation 2. Note that the "T'" on T'_{Do}, T'_R, and T'_E along the x-axis have been dropped for conciseness. In all panels, black bars are the FC response, red bars are the BF response, and blue bars are MF. These responses are averaged over respective regions of the Pacific ocean: the Northeast Pacific low cloud deck (15°N-40°N, 150°W-125°W) in panel a), the subtropical western Pacific (5°N-25°N, 150°E-155°W) in panel b), the Western Equatorial Pacific (5°S-5°N, 120°E-160°W) in panel c), and the Eastern Equatorial Pacific (5°S-5°N, 160°W-80°W) in panel d). The tropical average (20°S-20°N, 0°-360°) is presented in panel e) and the Eastern Equatorial Pacific with the tropical average subtracted out is presented in panel f). Figure S4 presents the SST diagnostic decomposition without grouped terms.

western half of the basin and this cooling signal extends nearly into the tropics. Considered together, we conclude that buoyancy forcing dominates the subtropical NH response of the ocean adjustment and positive feedbacks captured by BF act as a dynamic conduit by which extratropical cooling can reach the tropics.

3.2 Momentum-Driven Tropical Patterns

Though BF drives pattern formation in the subtropics and seems to provide a nearly zonally symmetric tropical surface cooling (Figure 1b), the La Niña and negative IOD zonal SST dipoles present in the tropical FC response (Figure 1a) are clearly a result of MF-driven surface cooling in the Eastern Equatorial Pacific (EEP) and the western equatorial Indian Ocean (Figure 1c). This image of MF-driven tropical pattern formation becomes even more clear in the profiles of near-surface equatorial (average of 5°S-5°N) temperature presented in Figures 1d-f. In FC, the Pacific and Indian basins feature strong zonal temperature dipoles: in the western Indian and EEP, cool temperature anomalies exist from the surface to depth (and well into the thermocline in the case of the Pacific), while the eastern Indian and Western Equatorial Pacific (WEP) are characterized by subsurface warm anomalies.

These zonal dipoles are reminiscent of the so-called "tilt-mode" often discussed in ENSO dynamics (e.g., Meinen & McPhaden, 2000; Bunge & Clarke, 2014), whereby changes in equatorial wind stress and resulting Ekman forcing drive a tilting of the main thermocline. Sure enough, comparison of the FC and MF profiles in Figures 1d and 1f confirms that the western Indian and EEP surface cooling and the eastern Indian and WEP subsurface warming so prominent in FC are momentum-driven responses. We treat the potential density isopycnal $\sigma_0 = 25$ kg m^{-3} as a proxy for the thermocline and plot climatological isopycnals (black line) in Figures 1d-f: the forced isopycnals (not shown) exhibit a tilt relative to the control, shoaling in the western Indian and EEP and deepening in the eastern Indian and WEP. This MF-driven thermocline tilt is in contrast to the equatorial BF profile where the $\sigma_0 = 25$ kg m^{-3} isopycnal shoals in all three basins. This widespread shoaling of the thermocline seen in BF is consistent with expectations: we expect an adiabatic isopycnal response to cooling as denser water classes move up in the water column. Considered in tandem, the widespread BF thermocline shoaling and the zonal dipole tilt from MF leads to a more pronounced thermocline shoaling in the western Indian and eastern Pacific and a more muted thermocline response in the eastern Indian and western Pacific.

At the equator, the BF mixed layer response is generally zonally symmetric. Within the Pacific thermocline, however, an unusual temperature dipole develops such that the eastern Pacific is cooler at depth than the western Pacific. Qualitatively, this BF subsurface cooling, which is likely a result of buoyancy-forced STC adjustment (Luongo et al., In Press), agrees with the results of Tseng et al. (Submitted). We leave the specific details of this buoyancy-forced tropical adjustment to a future study.

Forced thermocline vertical displacements by both BF and MF lead to surface temperature anomalies, and our mixed layer decomposition allows us to attribute the dynamic processes at play. WEP cooling (Figure 2c) largely follows the subtropical western Pacific: stronger wind speeds in BF increase evaporative cooling and primarily drive the total cooler FC response. In the EEP, however, different dynamics are at play (Figure 2d). While the total T' response is still driven by BF (in large part from T'_E's evaporative cooling from increased trade winds), the T'_{Do} response associated with BF and MF plays an increased role in setting EEP SST. In the EEP, zonal currents, meridional Ekman advection off the equator, and subsequent equatorial upwelling set climatological conditions, so it isn't necessarily surprising that ocean heat transport features prominently in the EEP's temperature response. Because the strong, nearly zonally symmetric BF cooling observed in Figures 1b and 1e obscures the local ocean adjustment at play in the EEP, we consider the EEP response relative to the rest of the tropics. Following Kang et al. (2019, 2020), we subtract out the tropical mean (average of 20°S-20°N) response, of which the mean pattern is strongly a function of BF (Figure 2e), to examine the EEP relative to the rest of the tropics (Figure 2f).

With this view, the total FC cooling is primarily a result of MF, specifically changes in ocean heat transport and increases in wind speed tempered by shortwave changes. To understand the ocean adjustment processes at play, we consider an advective decomposition (e.g., Yu & Pritchard, 2019; Wang et al., 2018; Kang et al., 2020; Luongo et al., In Press) of ocean heat transport changes ($\vec{u}\cdot\nabla T = u\,\partial T/\partial x + v\,\partial T/\partial y + w\,\partial T/\partial z$) integrated from the surface to 65 m depth (the average mixed layer depth in the control climate's EEP) and then averaged over the EEP (Figure S5a) because the advective component describes most of the Q_{net} response in EEP (Figure S5b). Decomposing the total advective response to NH TOA forcing into zonal, meridional, and vertical components hints at the dynamic processes at play in MF. In particular, MF's zonal component drives the FC cooling response, a result of either altered currents or temperature gradients which potentially result from momentum-driven isopycnal tilting. The meridional and vertical components of MF, which also cool, could result from the increased strength of the momentum-driven STC response (Luongo et al., In Press; Tseng et al., Submitted), which affects meridional heat divergence and upwelling strength. Though MF is the largest factor in EEP cooling, buoyancy-forced ocean heat transport changes also contribute to the cooling. This mixed layer buoyancy-forced adjustment, and the subsurface adjustment seen in Figure 1b, merit further investigation. Kang et al. (2020), who use a different GCM, point to vertical subsurface temperature changes as the driver of the La Niña pattern. We note that regardless of the impetus of initial cooling, surface processes can maintain the quasi-equilibrium response.

4 Discussion

4.1 Tropical Mode Phase Estimation

In Section 3.2 (above) we diagnose momentum forcing as the dominant driver of the Pacific Ocean La Niña pattern and Indian Ocean negative IOD pattern. However, a further question is why MF leads to negative phases of ENSO and IOD variability specifically. In the momentum-driven Bjerknes feedback, the sign of equatorial zonal wind stress forcing, τ^x, determines whether equatorial waves propagate with upwelling or downwelling patterns. These equatorial waves lead to a specific thermocline adjustment associated with a specific phase of ENSO and IOD. In Figures 1a and b, we see that FC τ^x is westward in the WEP: easterly τ^x anomalies create anomalous upwelling Kelvin waves which lead to a shoaling of the thermocline in EEP. Similarly, positive τ^x anomalies over the eastern Indian Ocean lead to upwelling Rossby wave adjustment and thermocline shoaling in the western Indian Ocean.

We can take this exercise one step further: why is τ^x negative over WEP and positive over the eastern Indian Ocean? Due to our wind stress locking methodology, τ^x in FC and MF are approximately equal. As discussed at length in Section 3.1, however, the subtropical FC response is driven nearly entirely by BF. As a result, we argue that the anomalous large-scale patterns of τ^x in FC, and by extension MF, is set by subtropical

BF adjustment. The τ^x fields calculated by CESM's atmospheric component (thus not affected by our wind stress overriding approach) exhibit a strong pattern correlation value of 0.774 (Figures S6a-b), lending credence to our interpretation. In particular, the subtropical PMM pattern, seen so clearly in Figure 1b's near-surface wind field, serves as an extratropical boundary condition that provides momentum forcing to WEP in the FC response and leads to a La Niña-like SST response in EEP. The resulting strengthened Walker cell adjustment may then drive anomalous easterly τ^x over the Indian Ocean and lead to the negative IOD pattern. This recognition that subtropical BF provides a tropical input for MF is important: an understanding of large-scale BF patterns can lead to predictability of tropical MF modes. In a global warming analog, W. Liu et al. (2015) use an approximate wind stress locking method and similarly conclude that the IOD-like response to greenhouse forcing results from Bjerknes adjustment primed by WES forcing.

It's worth mentioning that this phase predictability does not seem to work well in the equatorial Atlantic. Sub-surface MF-driven cooling is present in the western tropical Atlantic (Figure 1f) in addition to a deeper eastern-basin intensified BF sub-surface cooling. While theoretically this pathway of three positive feedbacks (low cloud SST, WES, and Bjerknes) could exist in the Atlantic basin, we see no sign of an Atlantic Niña in Figure 1c. This may be the result of well-known strong biases in the tropical Atlantic (e.g. Richter & Xie, 2008; Richter et al., 2012). In addition, westerly anomalies from the Pacific's increased Walker circulation, which would lead to near-surface divergence over the EEP, may partly cancel the PMM's easterly anomalies such that the Atlantic's FC τ^x response leads to no clear response.

4.2 Robustness of Pathway Across ETINMIP

The magnitude of subtropical cloud feedbacks varies widely across GCMs (e.g., Zelinka et al., 2020; Forster et al., 2021). In this study, the proposed dynamic pathway which connects extratropical cooling with a tropical Indo-Pacific SST response occurs via three positive feedbacks: low cloud SST and WES in the subtropics and Bjerknes in the deep tropics (schematically shown in Figure S7). This involves cloud forcing, so we might expect the response to be highly-dependent on GCM choice. We test the robustness of this pathway across the seven ETINMIP member models by plotting the strength of the surface shortwave cloud radiative effect (SW CRE) in the northeast Pacific's low cloud deck,

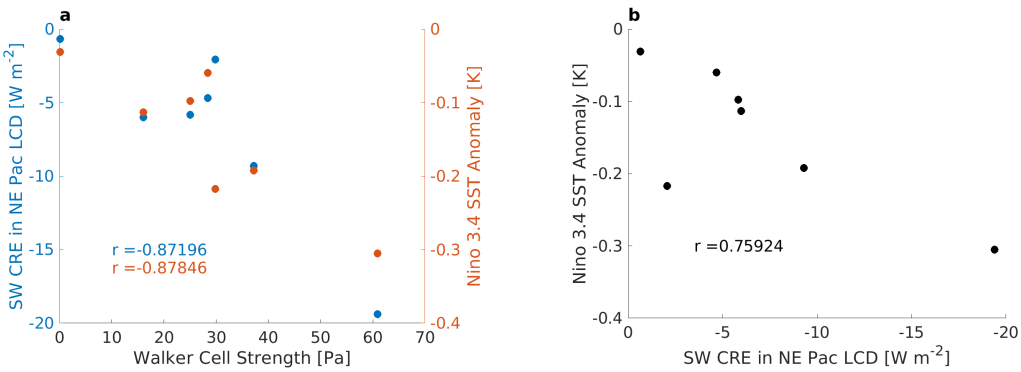

Figure 3. a) Scatter plot of the surface shortwave cloud radiative effect (SW CRE) response among seven ETINMIP member models (blue dots) vs. Walker circulation strength index, defined in Kang et al. (2020) as the sea level pressure difference over the central/east Pacific (5°S-5°N, 160°W-80°W) and the Indian Ocean/west Pacific (5°S-5°N, 80°E-160°E), and scatter plot of the Nino3.4 region (5°S-5°N, 170°W-120°W) SST response among seven ETINMIP member models (orange dots) vs. Walker circulation strength index. b) Scatter plot of SW CRE vs. Nino3.4 SST response among seven ETINMIP member models (black dots).

the Walker circulation index (defined as the difference between sea level pressure in the central/East Pacific, 160°-80°W, 5°S-5°N, and the Indian Ocean/west Pacific, 80°-160°E, 5°S-5°N: Kang et al., 2020), and the Nino 3.4 region (170°-120°W, 5°S-5°N) SST anomaly in Figures 3a and 3b. Strong correlations exist among the models between dynamically linked quantities, SW CRE and Walker cell strength and Nino3.4 SST and Walker cell strength; both relationships exhibit Pearson correlation coefficients of $r > |0.87|$. Despite not being directly dynamically linked, the correlation between the starting point of our pathway, northeast Pacific low cloud deck SW CRE, and the endpoint, Nino3.4 SST, is also strong: $r = 0.759$.

Though the ETINMIP multi-model mean exhibits a La Niña response (Figure S8), a caveat to these correlations is that CESM exhibits far-and-away the strongest SW CRE, Walker cell strength, and Nino3.4 SST responses (furthest rightward dot in Figures 3a and 3b) and hence could be seen as driving this trend. Nevertheless, removing CESM still leads to a correlation of $r = -0.713$ between Walker cell strength and Nino3.4 SST response and $r = -0.662$ between Walker cell strength and SW CRE response, although the correlation between SW CRE and Nino3.4 SST drops to $r = 0.359$. All told, this suggests that this NH feedback pathway may be robust across ETINMIP member models: models with less of a SW CRE response in the northeast Pacific's marine stratiform regime exhibit less of a La Niña response in the EEP. In addition, a similar feedback pathway has also been proposed by Kim et al. (In Press) for the case of SH TOA forcing, lending support to this result.

5 Conclusions

In this study we have investigated a dynamic pathway by which NH extratropical TOA cooling can induce a tropical SST response. Our use of wind stress locked GCM simulations has allowed us to partition the ocean-atmosphere adjustment into buoyancy forcing alone and momentum forcing alone, and we then use an ocean mixed layer decomposition to diagnose and dynamically attribute SST responses in several key regions of the Indo-Pacific. We have found that buoyancy forcing largely dominates in the subtropical Pacific; in particular, the positive low cloud feedback creates strong SST anomalies in the northeast subtropical Pacific low cloud deck, and these anomalies are translated southwestward to the tropics via wind speed driven evaporative cooling (the WES feedback). This thermodynamically driven low cloud-WES mode response is qualitatively similar to simulations that use slab ocean models (e.g., Kang et al., 2020; Hsiao et al., 2022; Tseng et al., Submitted). However, in dynamic ocean model simulations, these forced subtropical patterns provide an input to the tropics: anomalous easterlies in the WEP lead the Bjerknes feedback in MF to create zonal SST dipoles in the Pacific and Indian Oceans and create the familiar La Niña and negative IOD patterns. These patterns in the EEP are created through ocean heat transport changes primarily as a dynamic response to momentum forcing, though buoyancy forcing also factors into the dynamic response.

While the forced response of the tropical Atlantic merits further investigation, we highlight the utility of wind stress locking to predict the phase of equatorial mode responses to anomalous interannual to decadal forcing. These methods could be employed to understand the tropical Indo-Pacific SST quasi-equilibrium response to climate change and any subsequent downstream effects on global climate variability due to teleconnections between the tropical Pacific and the extratropics. While CESM seems to be an outlier in the strength of its atmosphere-ocean coupling, and thus its positive feedback strength, this pathway of three positive feedbacks seems to be somewhat robust across ETINMIP member models and is suggestive of a dynamic conduit connecting extratropical forcing to tropical variability.

6 Open Research

Online archiving of the GCM simulation data originally presented in Luongo et al. (In Press) and used to create Figures 1 & 2 of this manuscript is underway. The wind stress overriding protocol for CESM will be made available on MTL's Github and simulation data will be made available on Figshare. For this initial submission, the data has been uploaded as supporting information. The ETINMIP TOA insolation reduction CESM code and the long-term ETINMIP data used to create Figure 3 is available upon request from the authors of Kang et al. (2019).

Acknowledgments

This work was supported by National Science Foundation (NSF) grants 2048590 and 1934392. In addition, MTL is supported by a NASA FINESST Fellowship. We thank UCAR and NSF for providing the graduate student allocation of core hours on Cheyenne that this research used and the ETINMIP group for making their NEXT experimental code and restart files available. Without implying their endorsement, we thank Shantong Sun, Mark England, and Qihua Peng for helpful discussions and suggestions.

References

Amaya, D. J. (2019). The Pacific meridional mode and ENSO: A review. *Current Climate Change Reports*, *5*(4), 296–307.

Bjerknes, J. (1969). Atmospheric teleconnections from the equatorial Pacific. *Monthly Weather Review*, *97*(3), 163–172.

Bunge, L., & Clarke, A. J. (2014). On the warm water volume and its changing relationship with ENSO. *Journal of Physical Oceanography*, *44*(5), 1372–1385.

Burls, N. J., Muir, L., Vincent, E. M., & Fedorov, A. (2017). Extra-tropical origin of equatorial Pacific cold bias in climate models with links to cloud albedo. *Climate Dynamics*, *49*(5), 2093–2113.

Chang, P., Zhang, L., Saravanan, R., Vimont, D. J., Chiang, J. C., Ji, L., ... Tippett, M. K. (2007). Pacific meridional mode and El Niño—Southern oscillation. *Geophysical Research Letters*, *34*(16).

Chiang, J. C., & Vimont, D. J. (2004). Analogous Pacific and Atlantic meridional modes of tropical atmosphere–ocean variability. *Journal of Climate*, *17*(21), 4143–4158.

Clement, A. C., Burgman, R., & Norris, J. R. (2009). Observational and model evidence for positive low-level cloud feedback. *Science*, *325*(5939), 460–464.

England, M. R., Polvani, L. M., Sun, L., & Deser, C. (2020). Tropical climate responses to projected Arctic and Antarctic sea-ice loss. *Nature Geoscience*, *13*(4), 275–281.

Forster, P., Storelvmo, T., Armour, K., Collins, W., Dufresne, J.-L., Frame, D., ... Zhang, H. (2021). The Earth's energy budget, climate feedbacks, and climate sensitivity. In *Climate Change 2021: The Physical Science Basis. Contribution of Working Group I to the Sixth Assessment Report of the Intergovernmental Panel on Climate Change.* Cambridge University Press.

Hasselmann, K. (1976). Stochastic climate models part I. Theory. *Tellus*, *28*(6), 473–485.

Heede, U. K., Fedorov, A. V., & Burls, N. J. (2020). Time scales and mechanisms for the tropical Pacific response to global warming: A tug of war between the ocean thermostat and weaker Walker. *Journal of Climate*, *33*(14), 6101–6118.

Hsiao, W.-T., Hwang, Y.-T., Chen, Y.-J., & Kang, S. M. (2022). The Role of Clouds in Shaping Tropical Pacific Response Pattern to Extratropical Thermal Forcing. *Geophysical Research Letters*, e2022GL098023.

Hurrell, J. W., Holland, M. M., Gent, P. R., Ghan, S., Kay, J. E., Kushner, P. J., ... others (2013). The Community Earth System Model: a framework for collaborative research. *Bulletin of the American Meteorological Society*, *94*(9), 1339–1360.

Hwang, Y.-T., Xie, S.-P., Deser, C., & Kang, S. M. (2017). Connecting tropical climate change with Southern Ocean heat uptake. *Geophysical Research Letters*, *44*(18), 9449–9457.

Kang, S. M., Hawcroft, M., Xiang, B., Hwang, Y.-T., Cazes, G., Codron, F., ... others (2019). Extratropical–Tropical Interaction Model Intercomparison Project (ETIN-MIP): Protocol and Initial Results. *Bulletin of the American Meteorological Society*, *100*(12), 2589–2606. doi: https://doi.org/10.1175/

BAMS-D-18-0301.1

Kang, S. M., Held, I. M., Frierson, D. M., & Zhao, M. (2008). The response of the ITCZ to extratropical thermal forcing: Idealized slab-ocean experiments with a GCM. *Journal of Climate*, *21* (14), 3521–3532.

Kang, S. M., Xie, S.-P., Shin, Y., Kim, H., Hwang, Y.-T., Stuecker, M. F., ... Hawcroft, M. (2020). Walker circulation response to extratropical radiative forcing. *Science Advances*, *6* (47), eabd3021.

Kay, J. E., Deser, C., Phillips, A., Mai, A., Hannay, C., Strand, G., ... others (2015). The Community Earth System Model (CESM) large ensemble project: A community resource for studying climate change in the presence of internal climate variability. *Bulletin of the American Meteorological Society*, *96* (8), 1333–1349.

Kim, H., Kang, S. M., Kay, J. E., & Xie, S.-P. (In Press). Subtropical Clouds Key to Southern Ocean Teleconnections to the Tropical Pacific. *Proceedings of the National Academy of Sciences*. doi: https://doi.org/10.1073/pnas.2200514119

Larson, S., & Kirtman, B. (2013). The Pacific Meridional Mode as a trigger for ENSO in a high-resolution coupled model. *Geophysical Research Letters*, *40* (12), 3189–3194.

Larson, S., & Kirtman, B. P. (2014). The Pacific meridional mode as an ENSO precursor and predictor in the North American multimodel ensemble. *Journal of Climate*, *27* (18), 7018–7032.

Liu, W., Lu, J., & Xie, S.-P. (2015). Understanding the Indian Ocean response to double CO2 forcing in a coupled model. *Ocean Dynamics*, *65* (7), 1037–1046.

Liu, Z. (1994). A simple model of the mass exchange between the subtropical and tropical ocean. *Journal of Physical Oceanography*, *24* (6), 1153–1165.

Lu, F., Liu, Z., Liu, Y., Zhang, S., & Jacob, R. (2017). Understanding the control of extratropical atmospheric variability on ENSO using a coupled data assimilation approach. *Climate Dynamics*, *48* (9-10), 3139–3160.

Luongo, M. T., Xie, S.-P., & Eisenman, I. (In Press). Buoyancy forcing dominates cross-equatorial ocean heat transport response to NH extratropial cooling. *Journal of Climate*, 1–46. doi: https://doi.org/10.1175/JCLI-D-21-0950.1

Ma, J., Xie, S.-P., & Xu, H. (2017). Contributions of the North Pacific meridional mode to ensemble spread of ENSO prediction. *Journal of Climate*, *30* (22), 9167–9181.

McCreary, J. P., & Lu, P. (1994). Interaction between the subtropical and equatorial ocean circulations: The subtropical cell. *Journal of Physical Oceanography*, *24*(2), 466–497.

Meinen, C. S., & McPhaden, M. J. (2000). Observations of warm water volume changes in the equatorial Pacific and their relationship to El Niño and La Niña. *Journal of Climate*, *13*(20), 3551–3559.

Nonaka, M., Xie, S.-P., & McCreary, J. P. (2002). Decadal variations in the subtropical cells and equatorial Pacific SST. *Geophysical Research Letters*, *29*(7), 20–1.

Nonaka, M., Xie, S.-P., & Takeuchi, K. (2000). Equatorward spreading of a passive tracer with application to North Pacific interdecadal temperature variations. *Journal of Oceanography*, *56*(2), 173–183.

Norris, J. R., & Leovy, C. B. (1994). Interannual variability in stratiform cloudiness and sea surface temperature. *Journal of Climate*, *7*(12), 1915–1925.

Norris, J. R., Zhang, Y., & Wallace, J. M. (1998). Role of low clouds in summertime atmosphere–ocean interactions over the North Pacific. *Journal of Climate*, *11*(10), 2482–2490.

Pegion, K. V., & Selman, C. (2017). Extratropical precursors of the El Niño–Southern Oscillation. *Climate Extremes: Patterns and Mechanisms*, *226*, 301.

Richter, I., & Xie, S.-P. (2008). On the origin of equatorial Atlantic biases in coupled general circulation models. *Climate Dynamics*, *31*(5), 587–598.

Richter, I., Xie, S.-P., Wittenberg, A. T., & Masumoto, Y. (2012). Tropical Atlantic biases and their relation to surface wind stress and terrestrial precipitation. *Climate dynamics*, *38*(5), 985–1001.

Stuecker, M. F., Timmermann, A., Jin, F.-F., Proistosescu, C., Kang, S. M., Kim, D., … others (2020). Strong remote control of future equatorial warming by off-equatorial forcing. *Nature Climate Change*, *10*(2), 124–129.

Thomas, E. E., & Vimont, D. J. (2016). Modeling the mechanisms of linear and nonlinear ENSO responses to the Pacific meridional mode. *Journal of Climate*, *29*(24), 8745–8761.

Tseng et al., H.-Y. (Submitted). Fast and Slow Responses of the Tropical Pacific to

Radiative Forcing in Northern High Latitudes. *Journal of Climate*.

Vimont, D. J., Wallace, J. M., & Battisti, D. S. (2003). The seasonal footprinting mechanism in the Pacific: Implications for ENSO. *Journal of Climate*, *16*(16), 2668–2675.

Wang, K., Deser, C., Sun, L., & Tomas, R. A. (2018). Fast response of the tropics to an abrupt loss of Arctic sea ice via ocean dynamics. *Geophysical Research Letters*, *45*(9), 4264–4272.

Wood, R. (2012). Stratocumulus clouds. *Monthly Weather Review*, *140*(8), 2373–2423.

Xie, S.-P., Deser, C., Vecchi, G. A., Ma, J., Teng, H., & Wittenberg, A. T. (2010). Global warming pattern formation: Sea surface temperature and rainfall. *Journal of Climate*, *23*(4), 966–986.

Xie, S.-P., & Philander, S. G. H. (1994). A coupled ocean-atmosphere model of relevance to the ITCZ in the eastern Pacific. *Tellus A*, *46*(4), 340–350.

Yu, S., & Pritchard, M. S. (2019). A strong role for the AMOC in partitioning global energy transport and shifting ITCZ position in response to latitudinally discrete solar forcing in CESM1. 2. *Journal of Climate*, *32*(8), 2207–2226.

Zelinka, M. D., Myers, T. A., McCoy, D. T., Po-Chedley, S., Caldwell, P. M., Ceppi, P., … Taylor, K. E. (2020). Causes of higher climate sensitivity in CMIP6 models. *Geophysical Research Letters*, *47*(1), e2019GL085782.

Supporting Information for "A Dynamic Pathway by which Northern Hemisphere Extratropical Cooling Elicits a Tropical Response"

Matthew T. Luongo[1], Shang-Ping Xie[1], Ian Eisenman[1], Yen-Ting Hwang[2], &

Hung-Yi Tseng[2]

[1]Scripps Institution of Oceanography, UC San Diego, La Jolla, CA

[2]Department of Atmospheric Sciences, National Taiwan University, Taipei, Taiwan

Contents of this file

1. Text S1 & S2
2. Table S1
3. Figures S1 to S8

Text S1: Ocean Mixed Layer SST Decomposition

We perform an energy budget analysis of the vertically-integrated ocean mixed layer (e.g., Xie et al., 2010):

$$\rho_0 C_p H \frac{\partial T}{\partial t} = Q'_{net} + D'_o$$

$$= Q'_{SW} + Q'_{LW} + Q'_{SH} + Q'_{LH} + D'_o \, . \quad \text{(S1)}$$

Seawater density (ρ_0, assumed to be constant), ocean heat capacity (C_p), mixed layer depth (H), and temperature tendency ($\partial T/\partial t$) are balanced by the sum of net surface heat flux perturbations, Q'_{net}, and divergence of three-dimensional ocean heat transport, D'_o. In the subtropics and tropics in a quasi-equilibrium state, $\partial T/\partial t \approx 0$ (Figure S5 and Text S2). Thus, the change in Q'_{net}, the sum of changes in shortwave (Q'_{SW}), longwave (Q'_{LW}), sensible (Q'_{SH}), and latent heat fluxes (Q'_{LH}), is approximately balanced by D'_o:

$$Q'_{net} \approx -D'_o \ . \tag{S2}$$

Evaporation dominates latent heat flux changes in the tropics and subtropics (i.e. $Q'_{LH} \approx -Q'_E$: Figure S2). The linearized bulk formula for evaporation depends on wind speed (W), relative humidity (RH), air-sea temperature gradient ($S = T_a - T$, where T_a is near-surface air temperature as opposed to SST, denoted in this derivation as T), and a Newtonian cooling term proportional to the SST anomaly:

$$Q_E = L_v C_E \rho_a W[1 - \mathrm{RH} \cdot e^{\alpha S}] q_0 e^{\alpha T} \tag{S3}$$

Here, q_0 is a constant and C_E is the evaporative transfer coefficient. We also take $\alpha \equiv \frac{L_v}{R_v T^2}$, dependent on latent heat of vaporization, L_v, the gas constant, R_v, and T, to be effectively constant (Zhang & Li, 2014). Because we're interested in the evaporative tendency, Q'_E, we take the derivative of the bulk formula with respect to time:

$$Q'_E = \frac{\partial Q_E}{\partial T} T' + \frac{\partial Q_E}{\partial W} W' + \frac{\partial Q_E}{\partial \mathrm{RH}} \mathrm{RH}' + \frac{\partial Q_E}{\partial S} S' \tag{S4}$$

$$\frac{\partial Q_E}{\partial T}T' = \alpha\left(L_v C_E \rho_a W[1-\mathrm{RH}\cdot e^{\alpha S}]q_0 e^{\alpha T}\right)T'$$
$$= \alpha\left(L_v C_E \rho_a q_0 W[1-\mathrm{RH}\cdot e^{\alpha S}]e^{\alpha T}\right)T' = \alpha\overline{Q_E}T' \quad \text{(S5)}$$

Differentiating the exponential yields the same Q_E from the mean state, which we call $\overline{Q_E}$ moving forward. This SST-driven response is Newtonian evaporative damping.

$$\frac{\partial Q_E}{\partial W}W' = L_v C_E \rho_a q_0[1-\mathrm{RH}\cdot e^{\alpha S}]e^{\alpha T} = \frac{\overline{Q_E}}{\overline{W}}W' \quad \text{(S6)}$$

The above wind-speed-driven adjustment is the wind-evaporation-SST feedback (Xie and Philander, 1994) and is often significant in heat flux pattern formation. Simple algebra gives us the RH and S terms as well.

$$\frac{\partial Q_E}{\partial \mathrm{RH}}\mathrm{RH}' = -L_v C_E \rho_a q_0 W e^{\alpha(T+S)} = \frac{-\overline{Q_E}}{e^{-\alpha\overline{S}}-\overline{\mathrm{RH}}}\mathrm{RH}' \quad \text{(S7)}$$

$$\frac{\partial Q_E}{\partial S}S' = \alpha L_v C_E \rho_a q_0 W \mathrm{RH} e^{\alpha(T+S)} = \frac{-\alpha\overline{Q_E}\,\overline{\mathrm{RH}}}{e^{-\alpha\overline{S}}-\overline{\mathrm{RH}}}S' \quad \text{(S8)}$$

Bringing it all together,

$$Q'_E = \alpha\overline{Q_E}T' + \frac{\overline{Q_E}}{\overline{W}}W' + \frac{-\overline{Q_E}}{e^{-\alpha\overline{S}}-\overline{\mathrm{RH}}}\mathrm{RH}' + \frac{-\alpha\overline{Q_E}\,\overline{\mathrm{RH}}}{e^{-\alpha\overline{S}}-\overline{\mathrm{RH}}}S' \quad \text{(S9)}$$

$$-D'_o \approx$$
$$Q'_{SW} + Q'_{LW} - \left(\alpha\overline{Q_E}T' + \frac{\overline{Q_E}}{\overline{W}}W' + \frac{-\overline{Q_E}}{e^{-\alpha\overline{S}}-\overline{\mathrm{RH}}}\mathrm{RH}' + \frac{-\alpha\overline{Q_E}\,\overline{\mathrm{RH}}}{e^{-\alpha\overline{S}}-\overline{\mathrm{RH}}}S'\right) + Q'_{SH} \quad \text{(S10)}$$

Because we're interested in diagnosing temperature changes, we can solve directly for T' since we have it in our Newtonian cooling evaporative term. We rearrange and normalize by the product of the mean evaporative heat flux and the Clausius-Clapeyron scaling. Thus, we write a diagnostic equation for SST anomalies in a region:

$$T' \approx \frac{D_o' + Q_{SW}' + Q_{LW}' - \frac{\overline{Q_E}}{\overline{W}}W' - \frac{-\overline{Q_E}}{e^{-\alpha\overline{S}} - \overline{\mathrm{RH}}}\mathrm{RH}' - \frac{-\alpha\overline{Q_E}\,\overline{\mathrm{RH}}}{e^{-\alpha\overline{S}} - \overline{\mathrm{RH}}}S' + Q_{SH}'}{\alpha\overline{Q_E}} \tag{S11}$$

$$T' \approx T_{D_o}' + T_{SW}' + T_{LW}' - T_{E,W}' - T_{E,RH}' - T_{E,S}' + T_{SH}' \tag{S12}$$

In Figure 2 of the main text, we group radiative terms, $T_R' = T_{SW}' + T_{LW}'$, remaining evaporative terms, $T_E' = T_{E,WS}' + T_{E,RH}' + T_{E,S}'$, and neglect T_{SH}' as small (Figure S2):

$$T' \approx T_R' + T_E' + T_{Do}' \ . \tag{S13}$$

Text S2: Advective Decomposition of D_o'

In the mixed layer decomposition presented in Text S1 and the main text, D_o' is inferred from CESM's atmospheric heat flux fields with the assumption that the temperature tendency is small. However, we can also solve for D_o' from ocean fields to understand what ocean terms are potentially driving the heat flux changes and to justify our approximation. Note that in this derivation we drop prime terms for simplicity.

D_o includes 3D advective and diffusive processes. Because seawater is approximately non-divergent ($\nabla \cdot \vec{u} = 0$), we write this as:

$$D_o = \nabla \cdot (\vec{u}T) + \nabla \cdot \vec{\kappa} = \vec{u} \cdot \nabla T + \nabla \cdot \vec{\kappa} \ . \tag{S14}$$

Following Equation S1,

$$
\begin{aligned}
-Q_{net} &= \vec{u} \cdot \nabla T + \left(\rho c_p \partial T / \partial t + \nabla \cdot \vec{\kappa} + \mathrm{Res}_{interp} + \mathrm{Res}_{Reynolds} + \mathrm{Res}_{linear} \right) \\
&= \vec{u} \cdot \nabla T + \mathrm{Res}\ . \qquad \text{(S15)}
\end{aligned}
$$

Above, we group small error terms which depart from this large-scale balance between net surface heat flux and 3D advection into a residual term, Res. Respectively in Equation S15, this term is comprised of the tendency term, parametrized mixing and submesoscale processes, interpolation issues introduced by the model's coupler when interpolating between atmospheric and ocean grids and interpolation issues introduced in our own post-processing, sub-monthly Reynolds terms, and any errors introduced by our linearization of latent heat flux into evaporation.

Figure S5 shows that in the Eastern Equatorial Pacific $-Q_{net} \approx D_o$ and the Res term is small. Thus we can understand changes in D_o primarily to be a result of changes in advection.

References

Kang, S. M., Hawcroft, M., Xiang, B., Hwang, Y.-T., Cazes, G., Codron, F., ... others (2019). Extratropical–Tropical Interaction Model Intercomparison Project (ETIN-MIP): Protocol and Initial Results. *Bulletin of the American Meteorological Society*, *100*(12), 2589–2606.

Kang, S. M., Xie, S.-P., Shin, Y., Kim, H., Hwang, Y.-T., Stuecker, M. F., ... Hawcroft, M. (2020). Walker circulation response to extratropical radiative forcing. *Science Advances*, *6*(47), eabd3021.

Luongo, M. T., Xie, S.-P., & Eisenman, I. (In Press). Buoyancy forcing dominates cross-equatorial ocean heat transport response to NH extratropial cooling. *Journal of Climate*.

Xie, S.-P., Deser, C., Vecchi, G. A., Ma, J., Teng, H., & Wittenberg, A. T. (2010). Global warming pattern formation: Sea surface temperature and rainfall. *Journal of Climate*, *23*(4), 966–986.

Zhang, L., & Li, T. (2014). A simple analytical model for understanding the formation of sea surface temperature patterns under global warming. *Journal of Climate*, *27*(22), 8413–8421.

Case Name	Run Length	Coupler Output	τ-Lock	Insolation Reduction
Clim1	51 yrs	✓	×	×
Clim2	50 yrs	✓	×	✓
Tau1S1	50 yrs	×	✓	×
Tau1S2	50 yrs	×	✓	✓
Tau2S1	50 yrs	×	✓	×

Table S1.

The five CESM cases that we run for each ensemble set, indicating the simulation length (Run Length), whether we output the surface wind stress (Coupler Output), whether we specify the surface wind stress from another run (τ-Lock), and whether we reduce the insolation from 45°-65°N (Insolation Reduction). The names of the last three simulations indicate whether the wind stress is specified from Clim1 (Tau1...) or from Clim2 (Tau2...) and whether the insolation is left at its default value (...S1) or reduced (...S2).

The FC response illustrates the freely-evolving, total climate response to our NH extratropical TOA perturbation relative to the fully-coupled control: FC = Clim2-Clim1. The BF response captures the forced response that results from radiatively-induced buoyancy anomalies where radiative forcing is applied but unforced wind stress is specified relative to the decoupled control run: BF = Tau1S2-Tau1S1. Finally, the MF response illustrates the forced response that results from wind-stress-induced momentum anomalies alone by comparing a simulation wind stress specified from Clim2, but without radiative perturbations to the decoupled control run: MF = Tau2S1-Tau1S1.

This table is based on Table 1 from Luongo et al. (In Press). See their methods for further details.

©American Meteorological Society. Used with permission. This preliminary version has been accepted for publication in the Journal of Climate and may be fully cited. The final typeset copyedited article will replace the EOR when it is published.

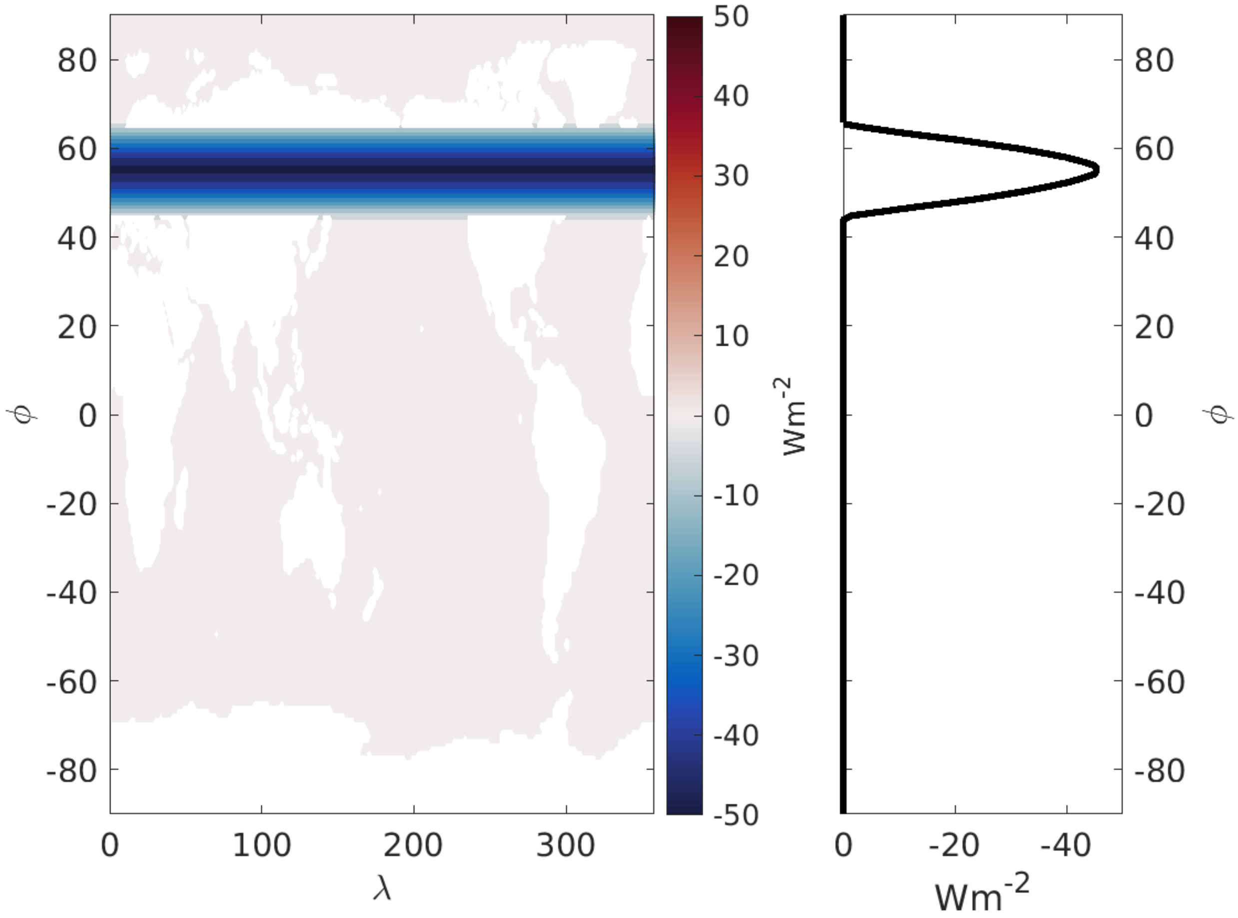

Figure S1. ETINMIP Northern Hemisphere Extratropics (Kang et al., 2019) annual-mean solar insolation perturbation applied in Clim2 and Tau1S2 experiments of this study. Left: Annual-mean solar insolation reduction as a function of latitude and longitude with contours of -5 Wm^{-2}. Right: Annual-mean, zonal-mean solar insolation reduction as a function of latitude. This figure is based on Figure S1 from Luongo et al. (In Press). ©**American Meteorological Society. Used with permission. This preliminary version has been accepted for publication in the Journal of Climate and may be fully cited. The final typeset copyedited article will replace the EOR when it is published.**

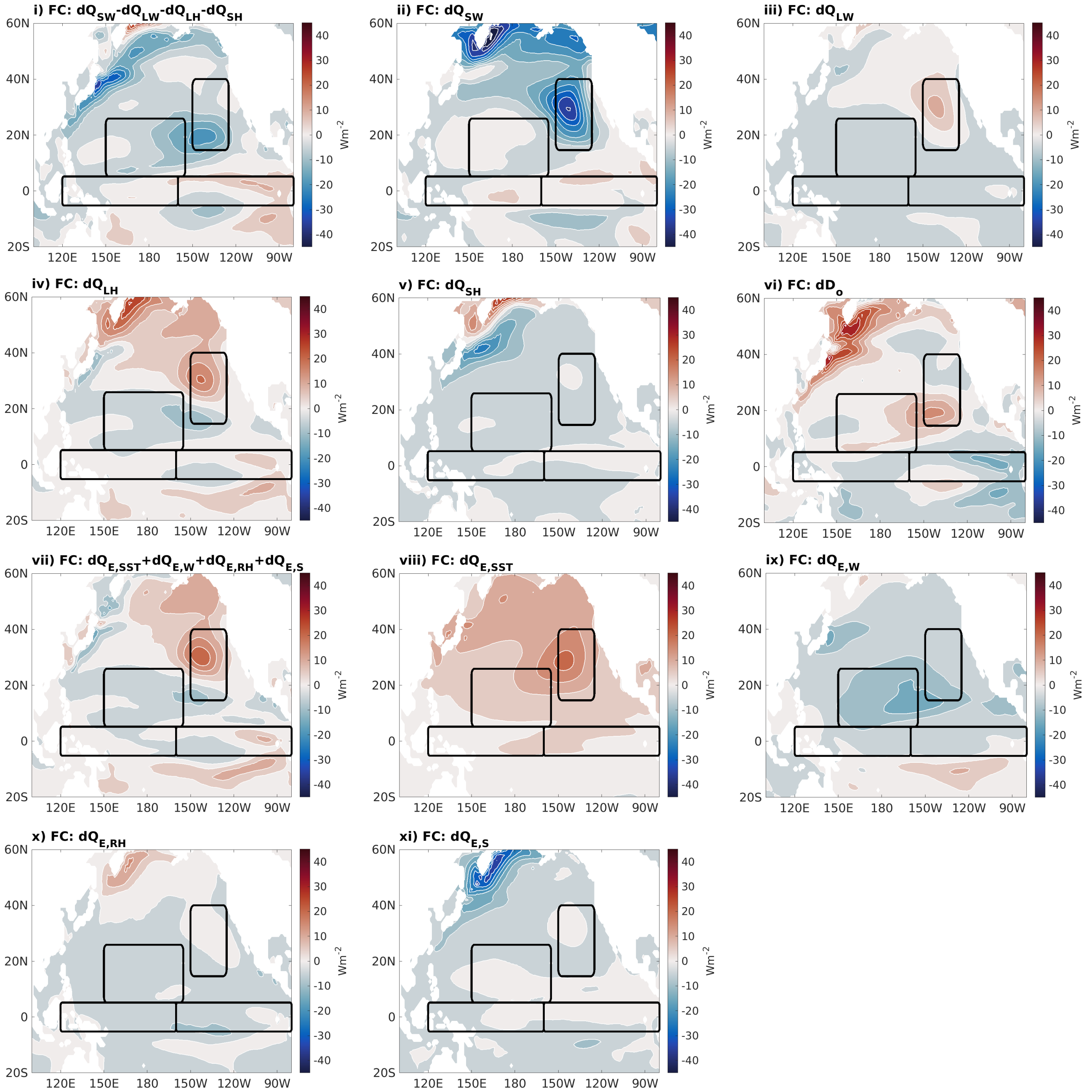

Figure S2a. FC: Following Equation 1 in the main text, Pacific Q'_{net} (i) decomposed into Q'_{SW} (ii), Q'_{LW} (iii), Q'_{LH} (iv), and Q'_{SH} (v). Q'_{net} is approximately balanced by D'_o (vi). In the midlatitudes and tropics, $Q'_{LH} \approx -Q'_E$ and the evaporative fields are given by $Q'_{E,SST}$ (viii), $Q'_{E,W}$ (ix), $Q'_{E,RH}$ (x), and $Q'_{E,S}$ (xi). The sum of these evaporative terms (viii-xi) given in (vii) which agrees well with (iv). Contours are 5 W m^{-2}.

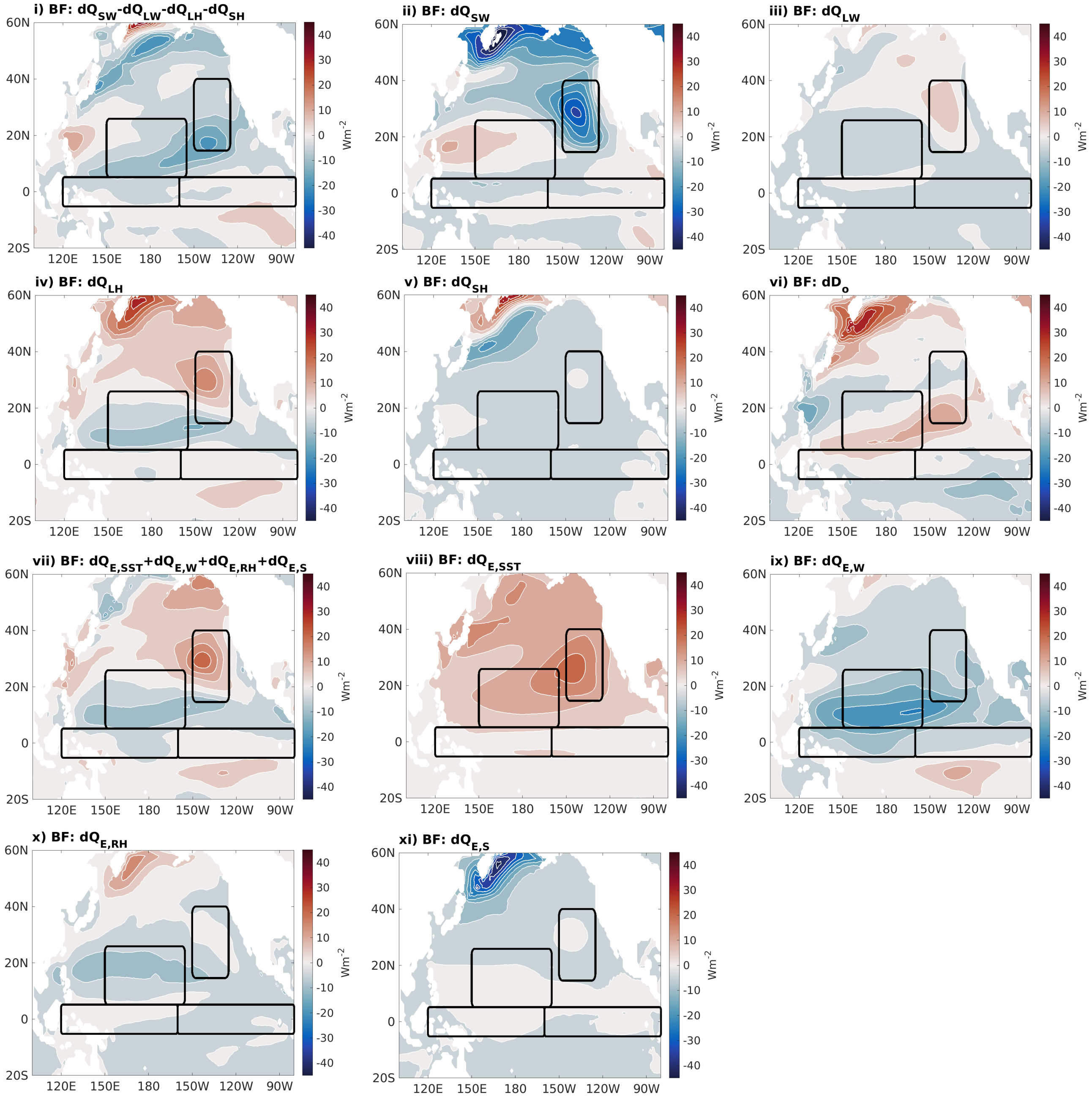

Figure S2b. BF: Following Equation 1 in the main text, Pacific Q'_{net} (i) decomposed into Q'_{SW} (ii), Q'_{LW} (iii), Q'_{LH} (iv), and Q'_{SH} (v). Q'_{net} is approximately balanced by D'_o (vi). In the midlatitudes and tropics, $Q'_{LH} \approx -Q'_E$ and the evaporative fields are given by $Q'_{E,SST}$ (viii), $Q'_{E,W}$ (ix), $Q'_{E,RH}$ (x), and $Q'_{E,S}$ (xi). The sum of these evaporative terms (viii-xi) given in (vii) agrees well with (iv). Contours are 5 W m^{-2}.

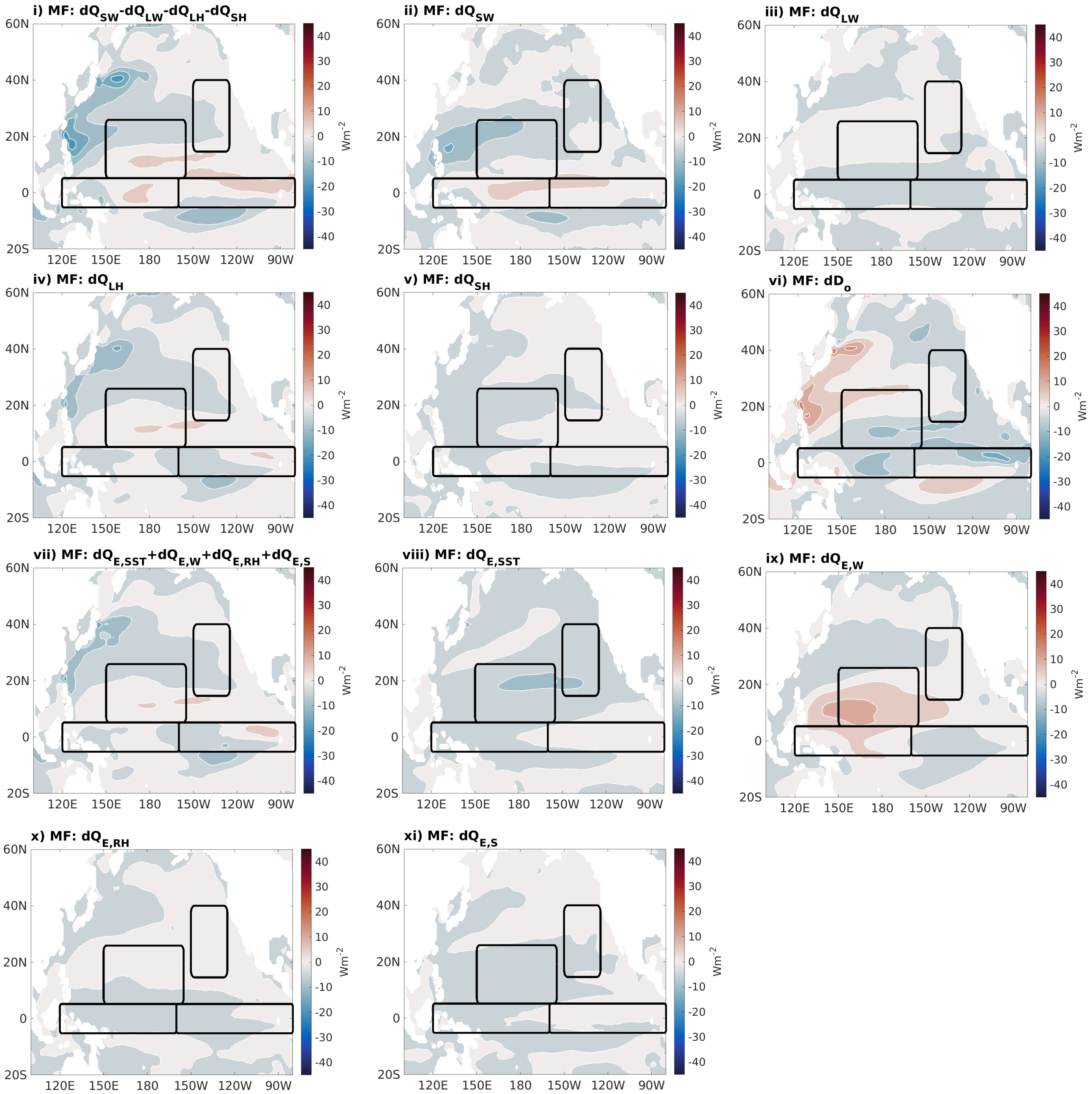

Figure S2c. MF: Following Equation 1 in the main text, Pacific Q'_{net} (i) decomposed into Q'_{SW} (ii), Q'_{LW} (iii), Q'_{LH} (iv), and Q'_{SH} (v). Q'_{net} is approximately balanced by D'_o (vi). In the midlatitudes and tropics, $Q'_{LH} \approx -Q'_E$ and the evaporative fields are given by $Q'_{E,SST}$ (viii), $Q'_{E,W}$ (ix), $Q'_{E,RH}$ (x), and $Q'_{E,S}$ (xi). The sum of these evaporative terms (viii-xi) given in (vii) which agrees well with (iv). Contours are 5 W m^{-2}.

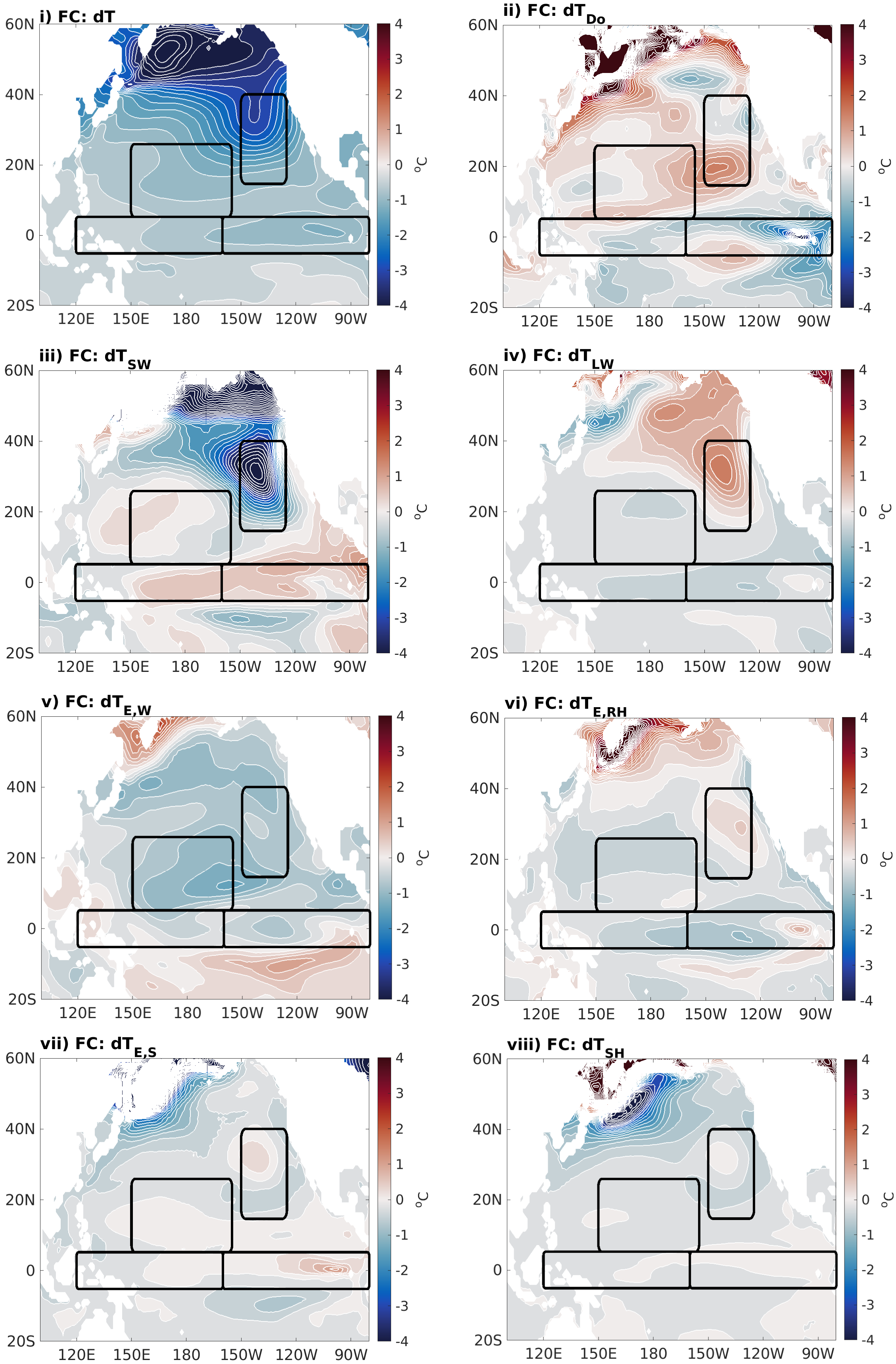

August 8, 2022, 11:58pm

Figure S3a. Basin-wide SST decomposition given in Equation 2 of the main text for the FC response. Contours are every 0.25 °C.

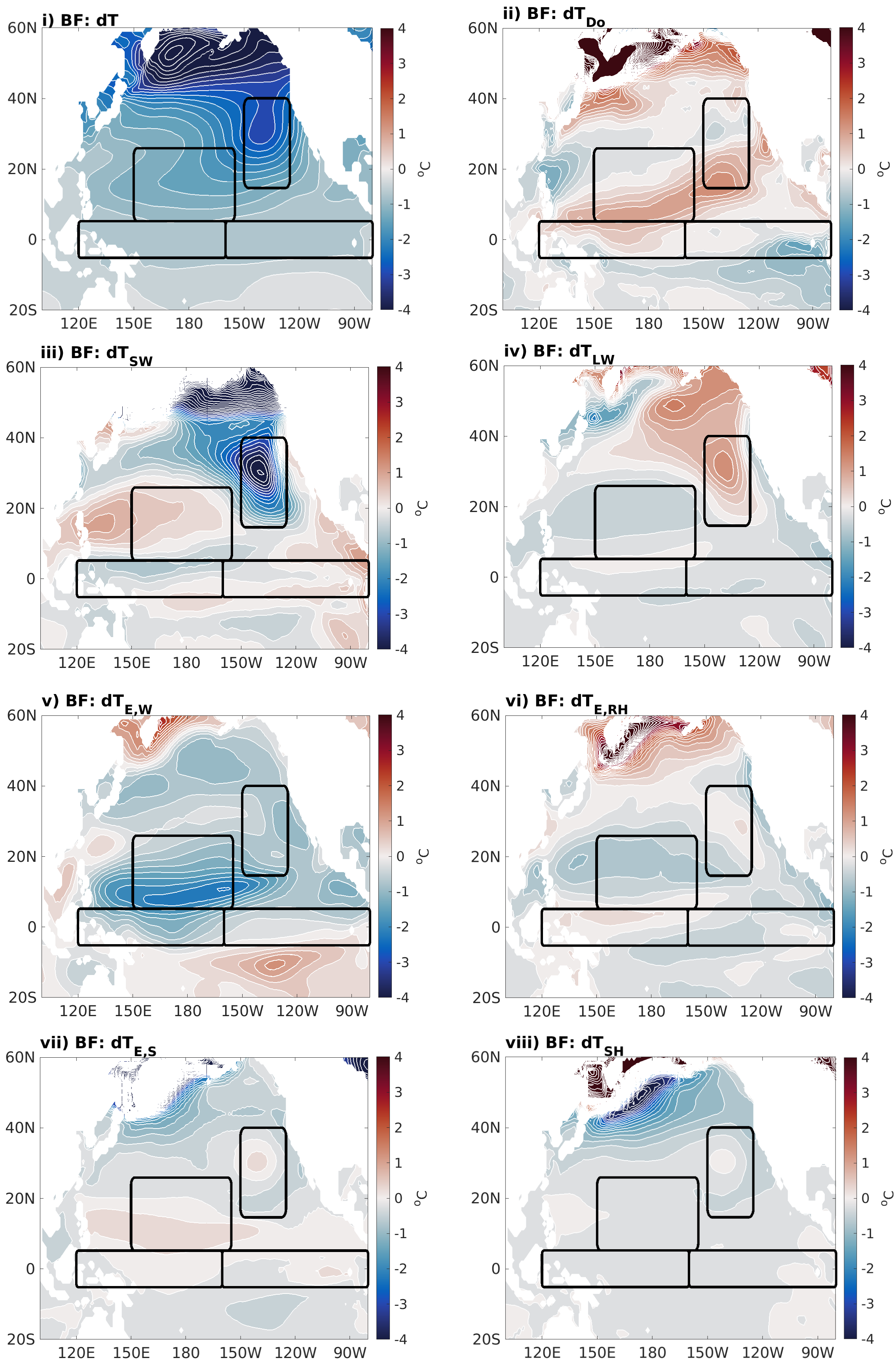

Figure S3b. Basin-wide SST decomposition given in Equation 2 of the main text for the BF response. Contours are every 0.25 °C.

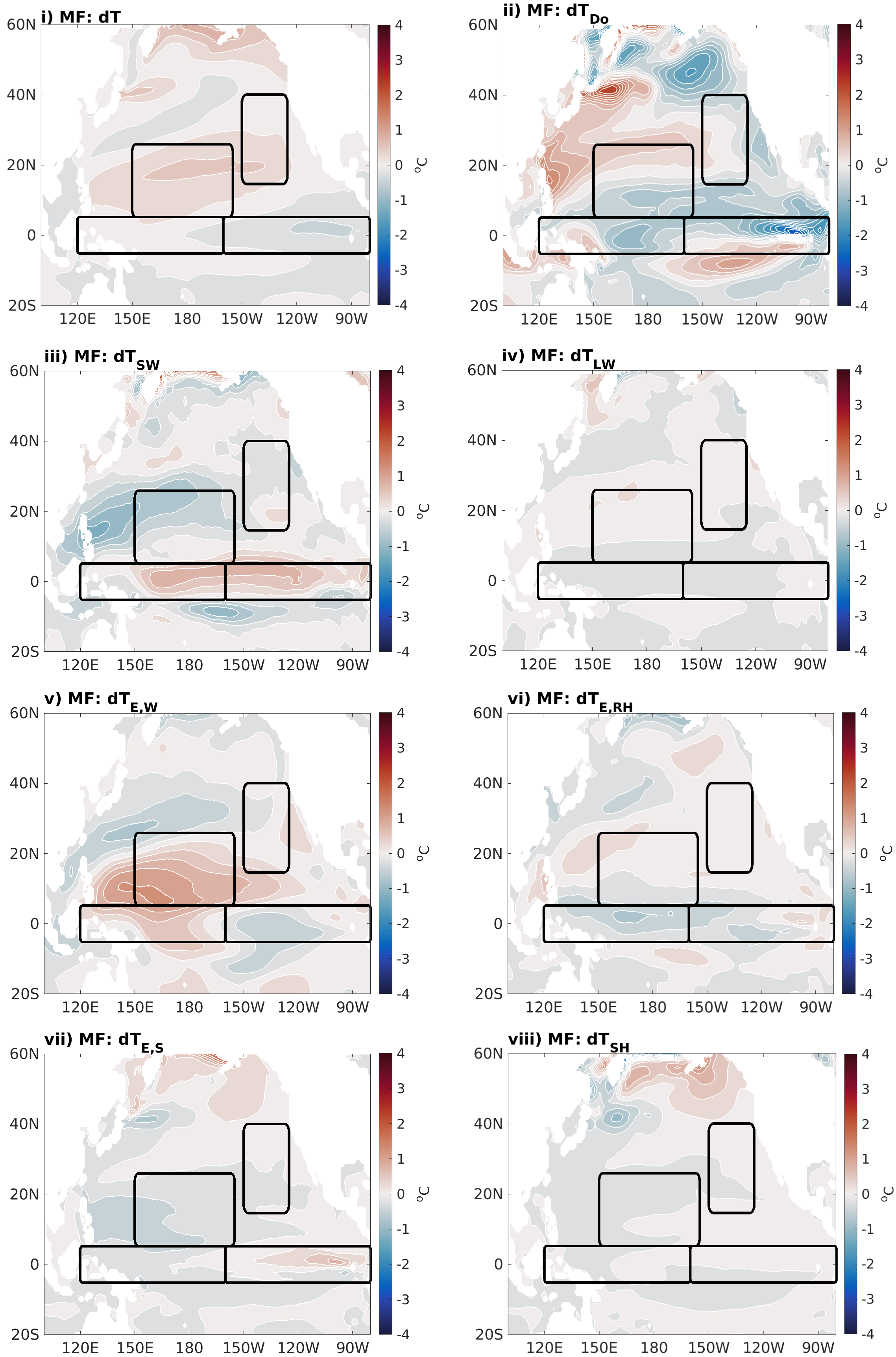

Figure S3c. Basin-wide SST decomposition given in Equation 2 of the main text for the MF response. Contours are every 0.25 °C.

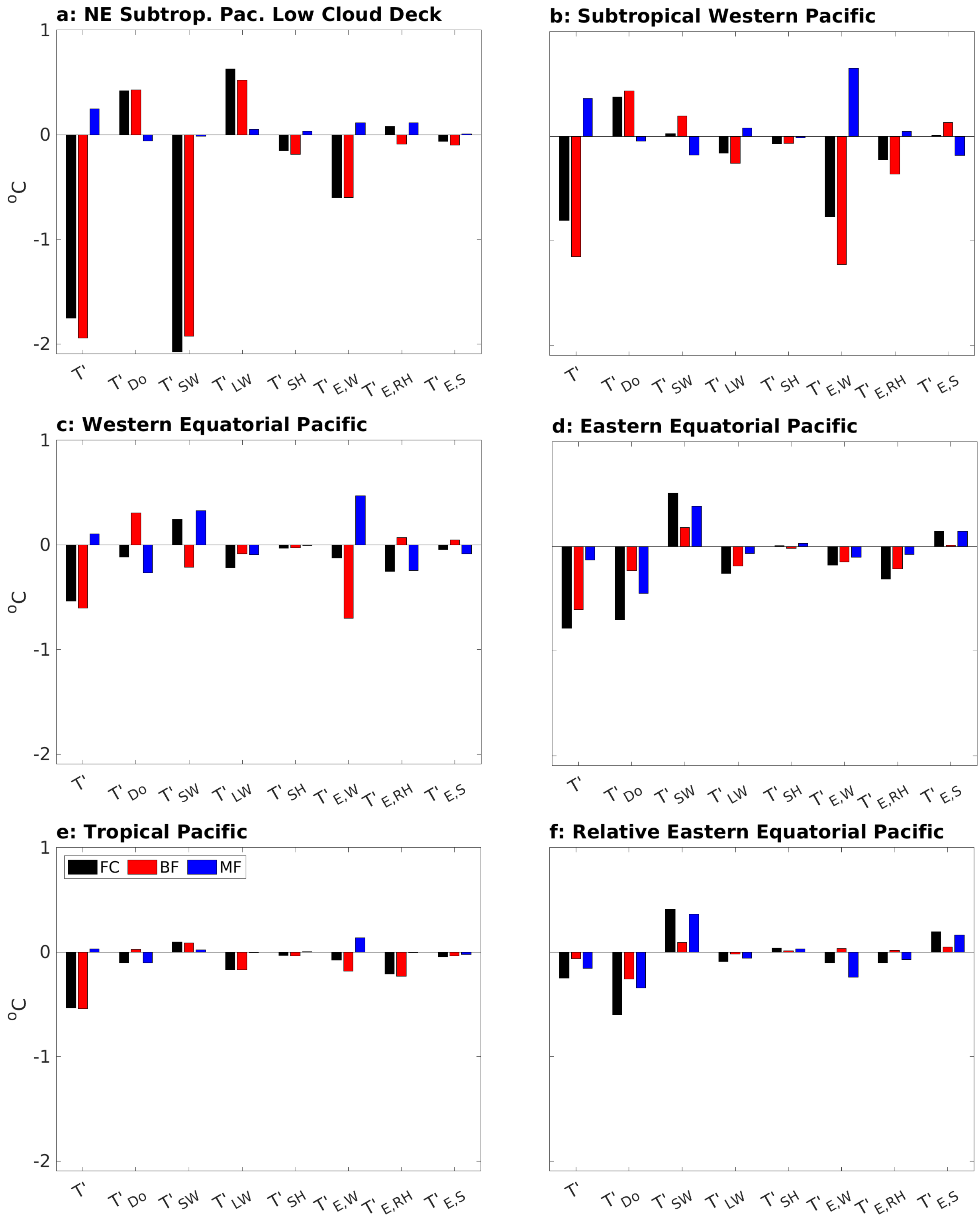

Figure S4. Area-averaged SST decomposition given in Equation 2 of the main text with all terms included.

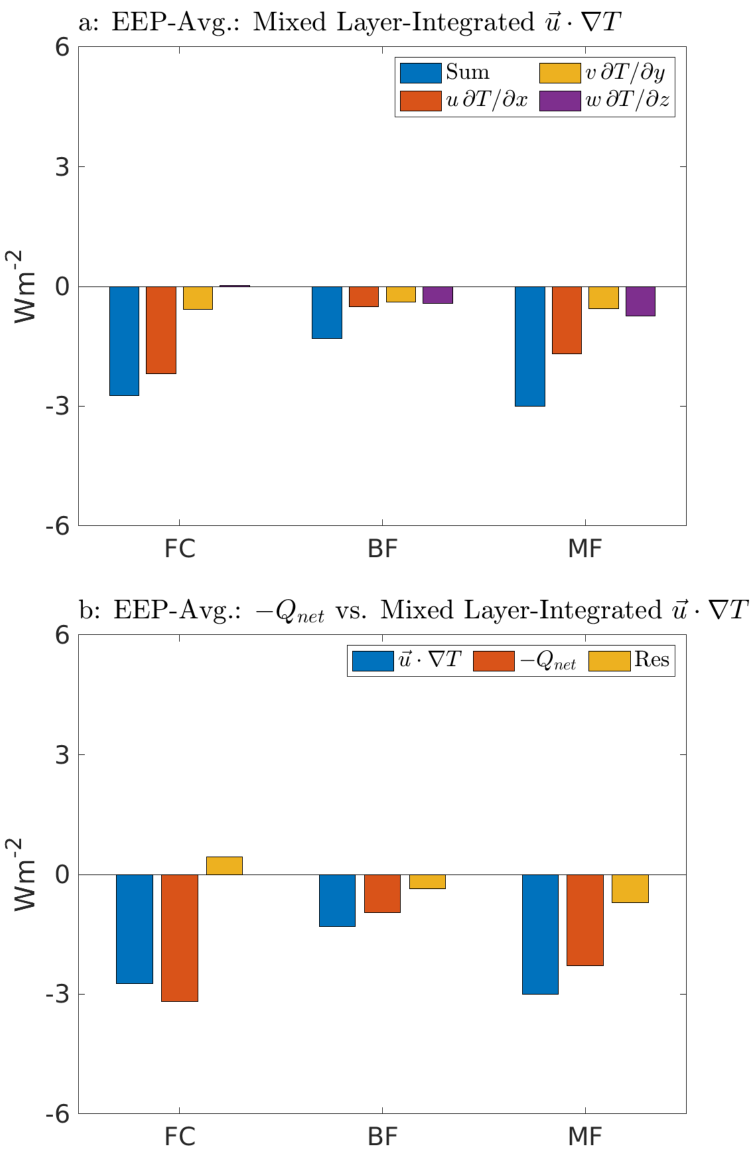

Figure S5. a): 3-D advective decomposition of ocean heat transport changes ($\vec{u} \cdot \nabla T = (u\,\partial T/\partial x + v\,\partial T/\partial y + w\,\partial T/\partial z)$ integrated from the surface to 65 m and averaged over the EEP (5°S-5°N, 160°W-80°W). 65 m is the average mixed layer depth over the EEP in the time mean of Clim1. b): Comparison between $-Q_{net}$ and the advective component of D_o. The difference between the two terms, Res, compares how well we can understand heat flux changes as a result of changes in advection. See Text S2.

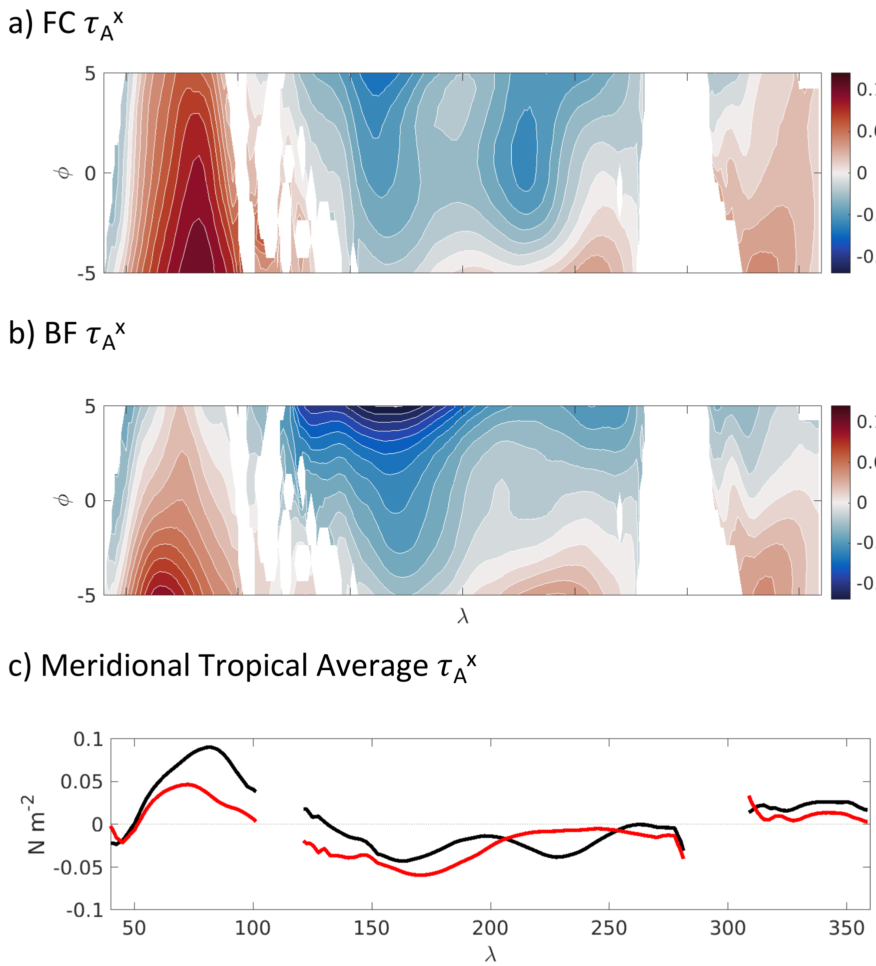

Figure S6. a): Atmospheric zonal wind stress, τ_A^x, as calculated by CESM's atmospheric component for the tropics in the FC case. Contours are 0.01 N m^{-2}. b): τ_A^x as calculated by CESM's atmospheric component for the tropics in the BF case. c): τ_A^x averaged over the equatorial region (5°S-5°N) for FC (black line) and BF (red line). The pattern correlation between panels a) and b) is r = 0.774

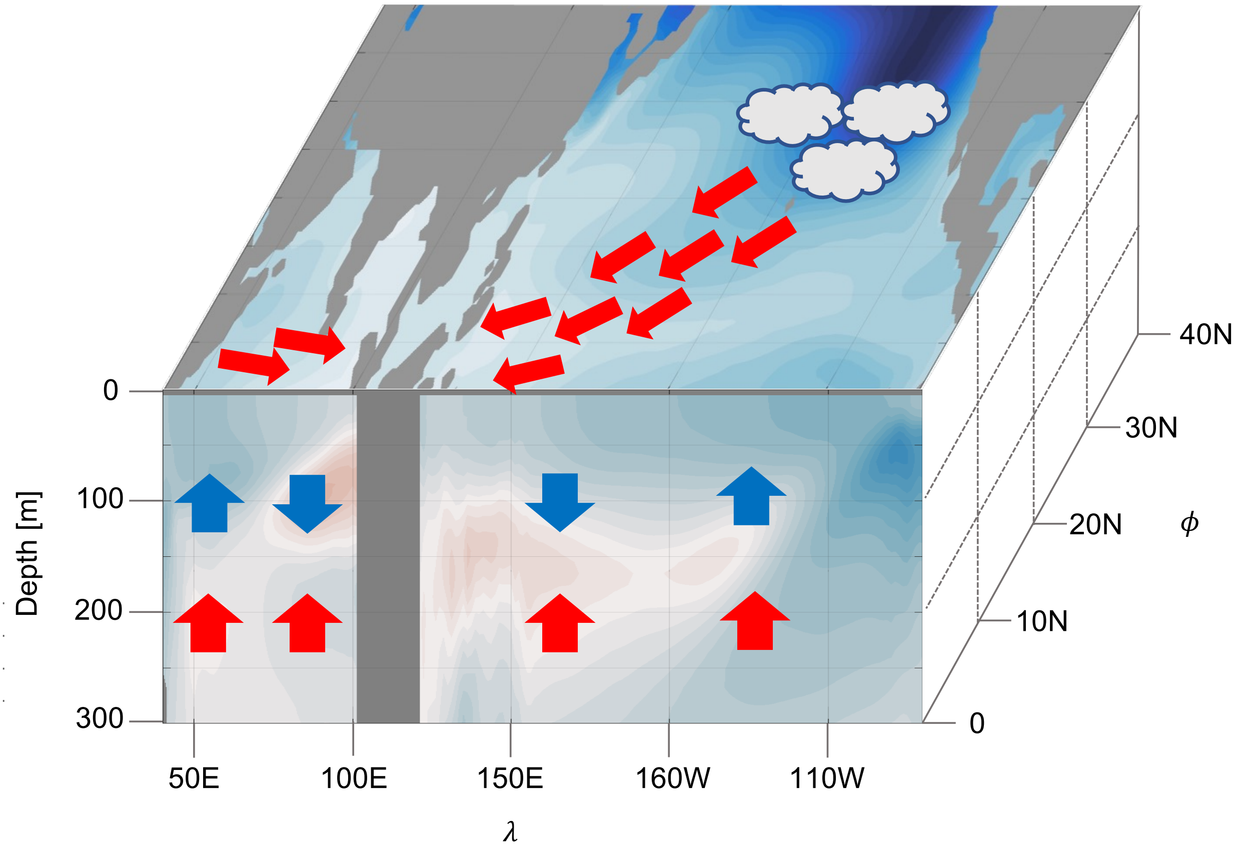

Figure S7. Schematic of proposed subtropical-to-tropical feedback pathway. In the NE subtropical Pacific, the SW cloud feedback amplifies SST anomalies which are carried southwestward to the tropics in a PMM pattern via the WES feedback (thin red arrows). This anomalous easterly wind stress in the Western Equatorial Pacific leads to a tilting tropical thermocline response in MF (thick blue arrows). The widespread cooling also leads to a universal thermocline shoaling (thick red arrows) in BF.

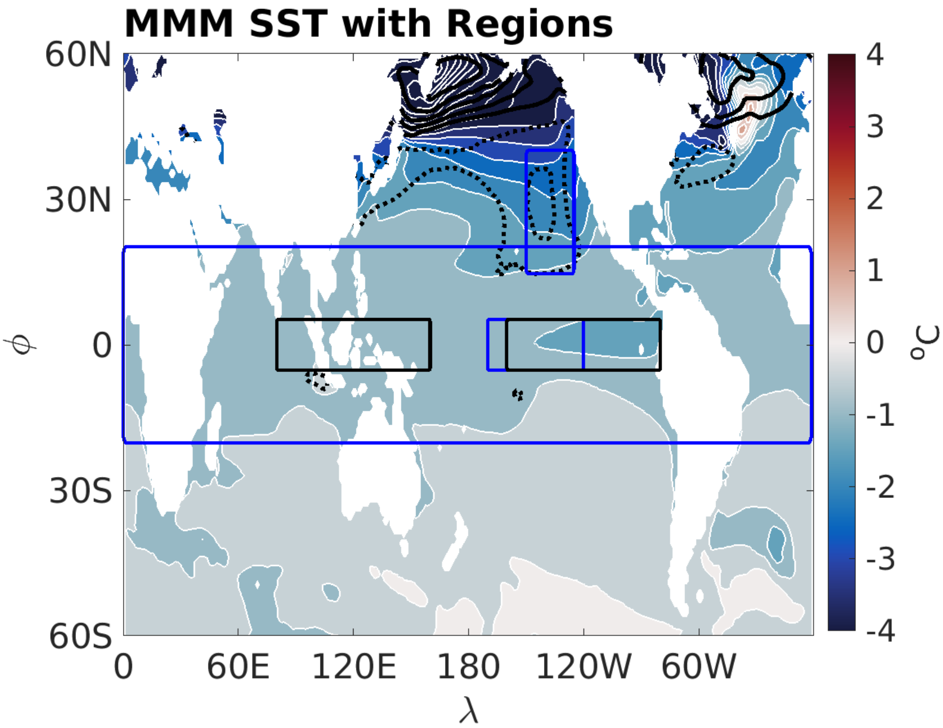

Figure S8. ETINMIP multi-model mean long-term response of SST (colorfill and white contours of 0.5 °C) and surface SW CRE reduction (black contours of 5 W m^{-2}, zero contour omitted, where solid is positive and dotted is negative). The black boxes in the equatorial region show the two areas which are compared to calculate Kang et al. (2020)'s Walker circulation strength index. The small blue box on the equator is the Nino3.4 region which is anomalized relative to the tropics (large blue box) by subtracting the large blue box average SST from it. The small subtropical blue box shows the northeast Pacific low cloud deck.